Materials Horizons

ROYAL SOCIETY OF CHEMISTRY

COMMUNICATION

View Article Online
View Journal

Cite this: DOI: 10.1039/d5mh02349a

Received 8th December 2025,
Accepted 13th April 2026

DOI: 10.1039/d5mh02349a

rsc.li/materials-horizons

An optically controlled synaptic device based on a $PdSe_2/\alpha\text{-}In_2Se_3$ vdW heterostructure FET

Anurag Ghosh, Inbar Dahan, Biswesweswar Santra, Gautham Vijayan, Michael Uzhansky and Elad Koren *

Visual synaptic devices show great promise for advanced neuromorphic hardware, offering a viable solution to the von Neumann bottleneck. However, achieving bidirectional optical control remains a considerable challenge. Herein, we demonstrate an all 2D heterostructure FET consisting of few-layer $PdSe_2$ and $\alpha\text{-}In_2Se_3$, designed as an optically controlled synaptic device with ferroelectric assisted tunability. The device emulates multiple forms of spike-dependent plasticity, exhibiting excitatory and inhibitory synaptic responses in the 642–980 nm and 406–520 nm spectral range, respectively. Moreover, the optically induced excitatory and inhibitory synapses can be modulated by an electrical gate pulse, utilizing the spontaneous polarization of $\alpha\text{-}In_2Se_3$. By leveraging the coupled ferroelectric and optical properties of In_2Se_3, the device exhibits an extended retention time of post-synaptic current (PSC) and enhanced device performance in terms of responsivity (R) and detectivity (D) compared with its $PdSe_2$-based counterparts. Logic gate operations (OR and AND) were demonstrated using 642 nm, 785 nm and 406 nm wavelengths as optical inputs. In addition, a three-layer artificial neural network (ANN) was trained to recognize a 28 × 28 pixel handwritten MNIST dataset by a back-propagation algorithm demonstrating high recognition accuracy of 96% and 97% under wavelengths of 642 nm and 406 nm, respectively. This study provides an effective strategy for the development of versatile optically controlled neuromorphic devices as fundamental building blocks for on-chip optical communication, optoelectronic logic, and Internet of Things (IoT) applications.

New concepts

Visual synaptic devices show great promise for advanced neuromorphic hardware, offering a viable solution to the von Neumann bottleneck. However, most of the reported visual synaptic devices involve hybrid manipulation approaches, which require both optical and electrical stimuli, introducing similar challenges such as complex device architecture, computational latency and high-power consumption. In this study, we demonstrate fully optical controlled operation using a 2D heterostructure neuromorphic device consisting of few-layer $PdSe_2$ and $\alpha\text{-}In_2Se_3$. In particular, the device emulates multiple forms of spike-dependent plasticity, with excitatory and inhibitory synaptic responses in the 642–980 nm and 406–520 nm spectral ranges, respectively. In addition, by leveraging the coupled ferroelectric and optical properties of In_2Se_3, the device exhibits an extended retention time of post-synaptic current (PSC) and enhanced device performance in terms of responsivity (R) and detectivity (D) compared with its $PdSe_2$-based counterparts.

Introduction

In recent years, substantial advancements in artificial intelligence (AI) have led to a growing demand for high-speed, low-power computational systems. The conventional von Neuman computing architecture faces inherent limitations in fulfilling these requirements due to its segregated design of the data receiver, processor, and memory units. This separation not only introduces latency but also exacerbates power consumption, posing challenges for next generation AI, big data, and the IoT.[1–3] On the other hand, functional diversification at the single device level has become essential to continue the down-scaling trend in the era of 'More than Moore'.[4] In recent years, extensive research has been focused on the development of neuromorphic based devices, with particular emphasis on visual synaptic operation to emulate human visual perception, memory, and logic at the single-device level.[5,6]

In the human neural system, sensory stimuli comes from the external world through various inputs such as vision, hearing, and smell, with the majority of ~80% being received through visual perception.[7,8] Similarly, artificial visual synapses have the potential to play a dominant role in sensory processing such as image recognition, smart detection and adaptation in real time with minimal power consumption.[3] However, most of the reported visual synaptic devices involve hybrid manipulation approaches with both optical and electrical stimuli, introducing similar challenges such as operational complexity, computational latency and high-power consumption, due to bandwidth-connection density trade-off.[2,5,9–16] For example, Wang *et al.*

Nanoscale Electronic Materials and Devices Laboratory, Faculty of Materials Science and Engineering, Technion – Israel Institute of Technology, Haifa 3200003, Israel. E-mail: eladk@technion.ac.il

demonstrated a retina-like vision sensor based on a van der Waals (vdW) heterostructure (HS) field-effect transistor (FET); in this device, a continuous gate bias was required to obtain a negative photoresponse for bipolar cell like functionality, which complicates device operation.[5] Conventionally, optical stimulation is associated with potentiation, representing the learning process, while electrical stimulation is linked to depression, corresponding to the forgetting process.[14,17,18] Inspired by the neural system from the human retina, a fully optical controlled synaptic device can overcome these challenges providing high bandwidth, low crosstalk, ultralow power consumption and simplified hardware design.[3,18–20] Such optically modulated synapses rely on positive photoconductivity (PPC) and negative photoconductivity (NPC) for potentiation and depression, respectively.[21] Recently, heterostructures composed of different non-layered materials as well as the integration of 2D materials with conventional bulk materials have been employed to realize all-optically controlled visual synapses such as IGZO/SnO/SnS, ZnAlSnO/SnO, perovskite/ZnO *etc.*[3,18,20,22,23]

Moreover, several studies have explored optically controlled visual synapses solely based on vdW materials, which can further utilize their exceptional optoelectronic properties and dangling-bond-free surfaces for advancing the downscaling trend in modern electronics.[2,4,24–29] In this regard, $PdSe_2$ has garnered significant attention due to its wavelength-dependent bidirectional photoresponse, high carrier mobility of 40 000 cm^{-2} V^{-1} s^{-1}, thickness-dependent bandgap (ranging from 1.3 eV for the monolayer to 0.03 eV for the bulk), and excellent air stability,[27,30] making it particularly advantageous for low power broadband photodetection applications across the UV to IR spectrum.[27,31] The reported synaptic operation in these devices primarily explained either through a charge trapping mechanism at the interface between the channel and substrate or *via* slow carrier recombination facilitated by oxidation-induced localized traps at the channel surface. Hence, the PSC exhibits volatile characteristics due to limited trapping strength and significant variability due to altered interfacial charactersitics.[26,27,32,33] In contrast, non-volatile synaptic memristors provide an excellent platform for maintaining long-term synaptic weights.[34] In particular, coupling interfacial trapped charges with ferroelectricity can significantly extend the retention time of PSC levels and enhance the functionality and performance of 2D based neuromorphic devices.[32,33,35] In this regard, α-In_2Se_3 has emerged as a promising material for neuromorphic applications, primarily due to its unique ferroelectric properties.[9,12,36–38] It exhibits room-temperature, intercoupled in plane (IP) and out of plane (OOP) ferroelectricity down to the monolayer limit alongside excellent optical properties.[39,40] In particular, its remanent polarization enables non-volatile memory (NVM) characteristics without requiring a continuous applied voltage,[41,42] where its direct bandgap and efficient light absorption, make it a suitable platform for multibit optical random access memory (O-RAM), in-memory sensing and logic applications utilized by streamlined read–write operations *via* a combination of optical and electrical pulses.[2,43]

Herein, we have integrated few layers of semiconducting $PdSe_2$ and ferroelectric In_2Se_3 to realize a bidirectionally optical controlled 2D synaptic device with ferroelectric assisted tunability. In this heterostructure, $PdSe_2$ serves as the FET channel, while In_2Se_3 acts as the virtual gate medium through dipole arrangements, modulating both the conducting state and photoresponse. In particular, the device demonstrates excitatory postsynaptic current (EPSC) and inhibitory postsynaptic current (IPSC) under illumination with wavelengths in the ranges of 642–980 nm and 406–520 nm, respectively. The device can effectively replicate all kinds of synaptic plasticity such as spike-duration-dependent plasticity (SDDP), spike-number-dependent plasticity (SNDP), spike-rate-dependent plasticity (SRDP), and intensity-dependent plasticity for both potentiation and inhibition. The EPSC at longer wavelengths arises from the PPC effect of both $PdSe_2$ and In_2Se_3, with In_2Se_3 predominantly generating electron–hole pairs due to its direct bandgap nature. Conversely, the IPSC is attributed to the NPC behaviour of $PdSe_2$, stemming from oxygen desorption and light-induced defect states under shorter wavelengths.[27,44] Moreover, intense 406 nm light can be employed to use the device in a reconfigurable manner by enabling a rapid RESET process. As a result, the device can be implemented and reconfigured for basic logic gate operations such as 'OR' and 'AND' solely by using visible light as input signals. In addition, the optically induced EPSC and IPSC can be further modulated with an electrical gate pulse leveraging the ferroelectric property of In_2Se_3. Based on the device characteristics, a simulation-based ANN was utilized to process a 28 × 28 pixel handwritten dataset using a backpropagation algorithm demonstrating a high recognition accuracy of 96% for 642 nm and 97% for 406 nm. The presented vdW HS device enables precise modulation of synaptic response by pulse amplitude, duration, and frequency of both optical and electrical signals, showcasing a promising platform for neuromorphic and optoelectronic applications.

Results and discussion

Device structure and characterization

In biological systems, neural networks consist of a vast array of hierarchically organized interconnected neurons communicating through synapses (Fig. 1a).[21] Depending on the input stimuli, the pre-synaptic membrane releases different types of neurotransmitters that results in either an EPSC or IPSC. An equivalent artificial synapse can be realized using a three-terminal FET architecture, where the channel functions as the synapse, and the channel current (I_D) represents the PSC. Presynaptic signals can be applied in the form of optical or electrical pulses. In our fabricated system the gate terminal was used as a modulatory input to regulate or attenuate the EPSC and IPSC induced by optical pulses.

To realize an optically controlled synaptic behaviour with an additional degree of freedom to modulate the optical synapse by gate actuation, an artificial synaptic FET is proposed based on an In_2Se_3–$PdSe_2$ heterostructure (Fig. 1b). α-In_2Se_3 was exfoliated using a conventional scotch tape method on a prepatterned conductive Si substrate coated with 300 nm thick SiO_2. Few-layer

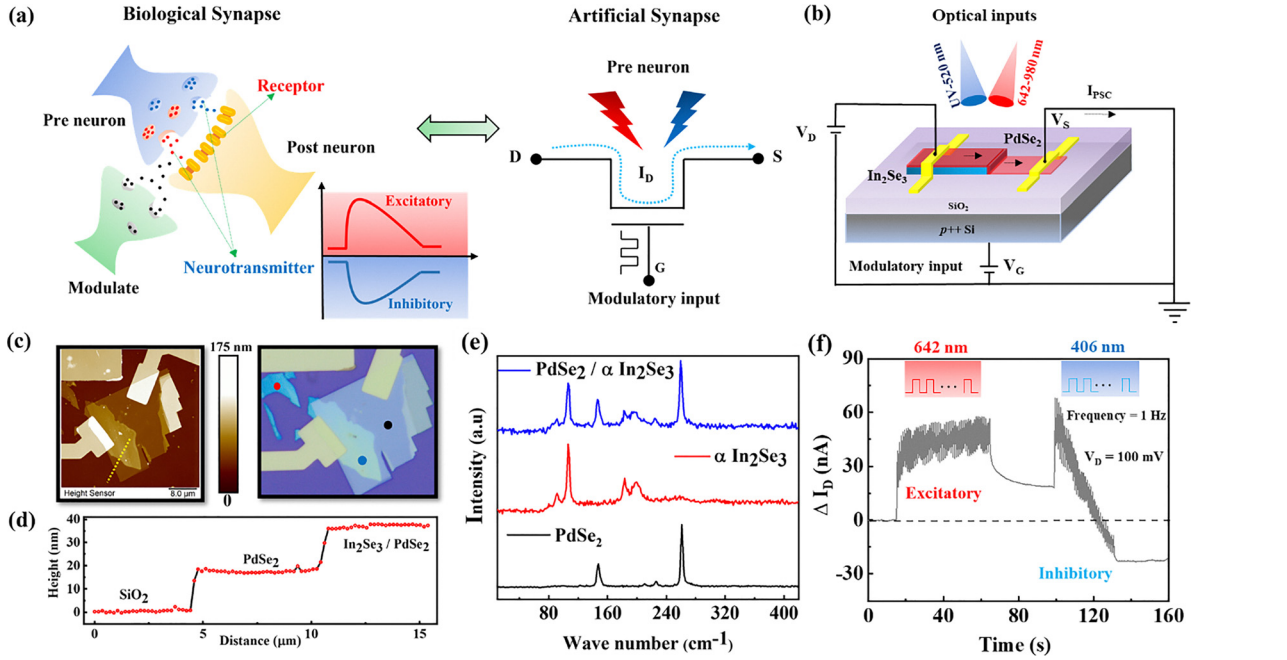

Fig. 1 (a) Schematic illustration of biological and artificial synapses. Two types of neurotransmitters determine the firing state of the post neuron being either excitatory or inhibitory. The generated EPSC or IPSC can be further controlled by the modulatory input. The equivalent artificial synapse of three terminal FET architecture where the PSC is primarily generated by the optical input and further modulated by the gate electrical input. (b) Schematic diagram of the $PdSe_2$–In_2Se_3 neuromorphic device. (c) Topographic and optical image of the device. (d) Height profile of the $PdSe_2$ and In_2Se_3 flakes. (e) Raman spectra of $PdSe_2$ (black spot in (c)), In_2Se_3 (red spot) and the heterostructure (blue spot). (f) Temporal photoresponse under successive illumination of 642 nm and 406 nm light pulses (frequency = 1 Hz, pulse width = 0.5 s).

$PdSe_2$ was exfoliated onto a PDMS stamp and subsequently transferred onto In_2Se_3 using a dry transfer method (see the Methods section). To achieve an asymmetric geometry, $PdSe_2$ was partially deposited over α-In_2Se_3,[45,46] enabling a balance between the PPC effect of α-In_2Se_3 and the NPC effect of $PdSe_2$. A comprehensive explanation of this configuration is provided in the Operation Mechanism section. In_2Se_3 was employed as a gate-switching medium, leveraging its ferroelectric properties, while $PdSe_2$ served as the FET channel. A global back gate was utilized for ferroelectric polarization modulation, and light illumination served as the primary input stimulus to regulate the PSC. $PdSe_2$ flakes with a thickness of 10–15 nm and In_2Se_3 flakes with a thickness of 15–20 nm were selected for device fabrication (Fig. 1c and d). Raman spectroscopy was conducted to assess the crystalline quality of the 2D flakes prior to the optoelectronic measurements (Fig. 1e). The Raman signals were collected from different regions of the device, as indicated in the optical micrograph of the device (Fig. 1c). The black spectrum represents pristine $PdSe_2$, exhibiting four characteristic peaks at ~147.1 cm^{-1}, ~210.7 cm^{-1}, ~226.7 cm^{-1}, and ~261 cm^{-1}, which correspond to the A_g^1–B_{1g}^1, A_g^2, B_{1g}^2, and A_g^3 vibrational modes, respectively.[27,31] The red spectrum corresponds to pristine In_2Se_3, which exhibits a sharp characteristic peak at ~106 cm^{-1}, attributable to the A_1 (LO + TO) phonon mode and two additional twin peaks, observed at ~183.4 cm^{-1} and ~199.4 cm^{-1} that are assigned to the A_1 (LO) and A_1 (TO) phonon modes, respectively. The LO–TO splitting of the A_1 mode provides well established evidence of centrosymmetry breaking and the emergence of ferroelectricity in In_2Se_3.[39,42,47] Additional direct evidence of non-volatile ferroelectric switching in α-In_2Se_3 using piezoelectric microscopy (PFM) measurements are shown in Fig. S1 and are in agreement with previous reports.[48–53] The blue spectrum represents the Raman signal from the overlapping region, where all the characteristic peaks of both In_2Se_3 and $PdSe_2$ are observed.

As discussed above, the device exhibits both potentiation (EPSC) and inhibition (IPSC) states using two characteristic wavelengths, 642 nm and 406 nm, respectively without relying on any additional electrical control. Fig. 1f illustrates the change in drain current following stimulation by multiple light pulses of 642 nm followed by 406 nm at a frequency of 1 Hz. A low read voltage of 100 mV (V_D) was applied to measure the drain current through the $PdSe_2$ channel. Closer inspection reveals that the device shows an instant PPC under 406 nm illumination, whereas I_D gradually decreases as the time of illumination is prolonged (Fig. S2). Additionally, the device demonstrates IPSC under 520 nm stimulation, although the rate of achieving the depression is milder compared to at 406 nm (Fig. S3a and b). Similarly, the device demonstrates potentiation characteristics under illumination extended up to 980 nm, as $PdSe_2$ is capable of sensing light within the infrared range as well (Fig. S3c).

Optically induced synaptic plasticity

To demonstrate that the device effectively replicates various forms of spike-dependent plasticity solely through optical stimulation for both potentiation and inhibition, two representative

wavelengths of 642 nm and 406 nm were selected. To demonstrate the variation from short-term plasticity (STP) to long-term plasticity (LTP), the device was exposed to 642 nm light illumination for 10 consecutive pulses of different durations with the same time interval (Fig. 2a). As the pulse duration increases from 10 ms to 500 ms, the PSC level (following the 10th pulse) increased from ~3.5 nA to ~18 nA. A similar behaviour was observed by varying the number of pulses (SNDP) while maintaining the same pulse duration (0.5 s) and frequency (1 Hz) (Fig. 2b) and by varying the light intensity (Fig. 2c). Fig. 2d depicts

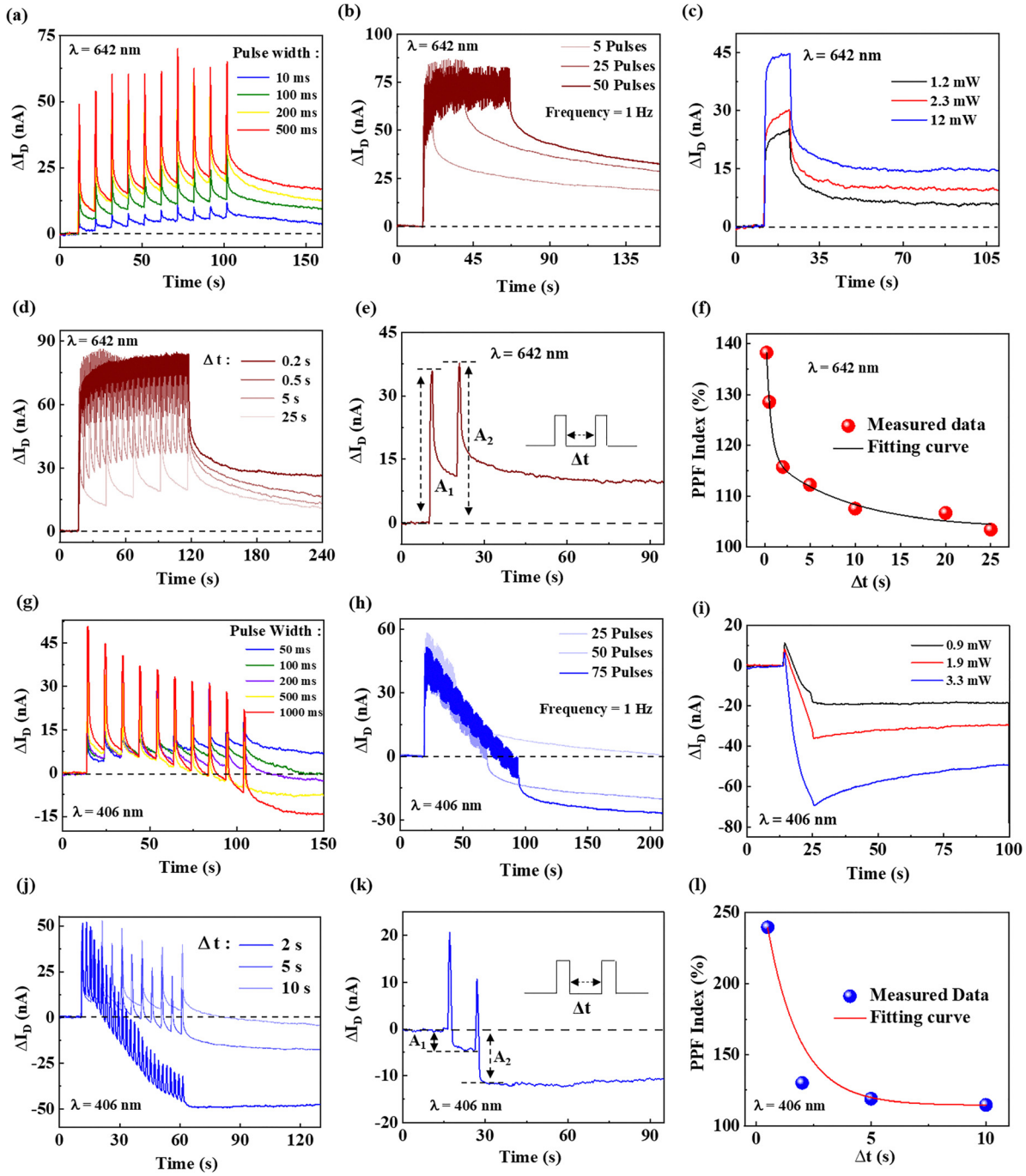

Fig. 2 (a) STP to LTP transition under illumination by varying pulse width of light at a wavelength of 642 nm. (b) EPSC triggered by a different number of 642 nm light pulses (pulse width = 0.5 s, frequency = 1 Hz). (c) EPSC triggered by varying intensities of 642 nm light with a pulse width of 10 s. (d) EPSC triggered by different pulse intervals (Δt) of 642 nm light (pulse duration = 1 s). (e) EPSC stimulated by two consecutive 642 nm light pulses at intervals of 10 s, where A_1 and A_2 represent the amplitude of photocurrent achieved after the 1st and 2nd pulse respectively. (f) PPF index as a function of pulse interval. (g) STD to LTD transition by different pulse widths of 406 nm light. (h) IPSC triggered by a different number of 406 nm light pulses (pulse width = 0.5 s, frequency = 1 Hz). (i) IPSC stimulated by different intensities of 406 nm light with pulse width of 10 s. (j) STD to LTD transition with different pulse intervals of 406 nm light. (k) IPSC stimulated by two consecutive 406 nm light pulses at 10 s intervals. (l) PPF index as a function of pulse interval.

the modulation from STP to LTP demonstrating SRDP by varying the time interval (Δt) between two consecutive pulses for a time duration of 100 s, while maintaining a constant pulse width of 1 s. In particular, the PSC level decreases from ~26 nA to ~10 nA, as Δt increases from 0.2 s to 25 s. To obtain further insight into the correlation between memory level and Δt, we have calculated the paired-pulse facilitation (PPF) index, which is a critical parameter used to characterize STP in biological synapses,[18,27] using the following equation:

$$\text{PPF index} = \frac{A_2}{A_1} \times 100\% \quad (1)$$

Here, A_1 and A_2 represent the amplitudes of the photocurrent corresponding to the first and second pulses, respectively, as illustrated in Fig. 2e. As shown in Fig. 2f, the PPF index exhibits an exponential dependence on Δt, aligning well with the principles of neurobiology.[3] The calculated data were fitted using the following equation:

$$\text{PPF index} = A_0 + C_1 \times \exp\left(-\frac{\Delta t}{\tau_1}\right) + C_2 \times \exp\left(-\frac{\Delta t}{\tau_2}\right) \quad (2)$$

where, C_1 and C_2 represent the initial magnitudes, while τ_1 and τ_2 denote the fast and slow relaxation time constants, respectively. Based on eqn (2), the extracted values of τ_1 and τ_2 were found to be 0.5 s and 8.78 s, respectively. Notably, the device achieved a maximum PPF index of 138% at Δt = 0.2 s, demonstrating its decent performance compared to recently reported studies.[3,18]

Analogous forms of synaptic plasticity associated with inhibitory responses were successfully demonstrated, as shown in Fig. 2g–l, indicating that the transition from short term depression (STD) to long term depression (LTD) can be achieved through 406 nm excitation. Notably, Fig. 2g, that illustrates SDDP, highlights the intriguing interplay between PPC and NPC under 406 nm exposure, where for the shortest pulse durations (50 ms), the device exhibits a small potentiation trend driven by the PPC effect. However, as the pulse duration increases, the NPC effect becomes dominant, leading to a depression state. This behaviour underscores the dynamic competition between two opposing photoconductive effects governing the synaptic response. Similarly, the PPF index associated with the inhibitory process under 406 nm stimulation is presented in Fig. 2h, where τ_1 and τ_2 are calculated to be 1.12 s and 1.36 s, respectively. These results emphasize the device versatility in emulating complex synaptic behaviours by using two representative wavelengths. Although bidirectional synaptic plasticity can be realized without the application of an external gate voltage, the polarization state of In_2Se_3 can be deterministically programmed by applying a gate-voltage pulse prior to optical stimulation enabling further tunability of the synaptic response, as discussed in the following section.

Polarization dependent optical synapse

The optically induced synaptic plasticity of the $PdSe_2$–In_2Se_3 device can be further modulated through electrical gate pulses, harnessed by the ferroelectric properties of In_2Se_3. Electric polarization dependent measurements were conducted for both 406 and 642 nm wavelengths following different gate induced poling conditions. In the first step, an electrical gate pulse of different amplitude and polarity was applied to align the dipoles in In_2Se_3. Following the poling process, a 2 min delay time was obtained before performing the I_D-t measurements with light pulses to minimize gate-induced trapping effects (Fig. S4a and b). Subsequently, the device was subjected to a series of light pulses at an interval of 10 s with a duration of 1 s. As shown in Fig. 3a, the photocurrent for 642 nm light illumination increases with the transition of gate poling conditions from negative to positive, resulting in higher PSC levels. Fig. 3b demonstrates the progressive increase in photocurrent for the 1st and 10th light pulses, rising from 19.8 nA to 50 nA and 23 nA to 62 nA, respectively as the poling condition changes from $-V_G$ to $+V_G$, resulting in enhanced EPSC. Additionally, the difference in photocurrent between the 1st and 10th pulse grows with positive gate voltage, corroborating the observation that under distinct poling conditions, the photocurrent requires different amounts of time to reach the saturation level. This demonstrates the capability to achieve distinct current levels for LTP, independent of pulse duration and frequency. Furthermore, the PPF function shows a clear linear dependence on the gate poling conditions for an identical input stimulus (Fig. S4c), enabling control of the potentiation level by applying an electrical gate pulse beforehand. Such linear behavior of the PPF was observed across all measured devices. The EPSC following two opposite poling conditions of ±90 V with various frequencies of light pulses is presented in Fig. S5, confirming that the variable current level for LTP can be effectively established by introducing an electrical gate pulse.

Similar gate modulation was observed associated with the IPSC under 406 nm exposure (Fig. 3c and Fig. S5f). In particular, a distinct level of LTD ranging from −3 nA to −15.6 nA is obtained depending on the gate induced poling conditions. It is important to note that for the IPSC (EPSC) measurements, the PSC levels following negative (positive) gate poling are rather closely spaced in comparison with those obtained following positive (negative) gate actuation. This can be clearly seen in the representative figures showing that the adjacent profiles representing opposite gate polarities are rather closely spaced. Therefore, for better visualization, we have included few representative profiles to show the effect of modulation. Complete datasets with uniform gate intervals are provided in Fig. S6. The device exhibits the highest levels of both IPSC and EPSC under positive poling attributed to the strongest photoresponse due to the dipole-induced band alignment of the heterostructure device (see further discussion below). As mentioned above, there is competition between PPC and NPC during the inhibition process, which is clearly observable in Fig. 3d. Although the photoresponse for both the 1st and 10th light pulses increases with positive gate poling, the photoresponse of the 10th pulse is lower than that of the 1st pulse for each poling condition. This indicates that the NPC effect from $PdSe_2$ becomes increasingly dominant with time until overcoming the PPC effect from In_2Se_3.

The presence of In_2Se_3 significantly enhances the overall photoresponse of the device and its intrinsic ferroelectric field

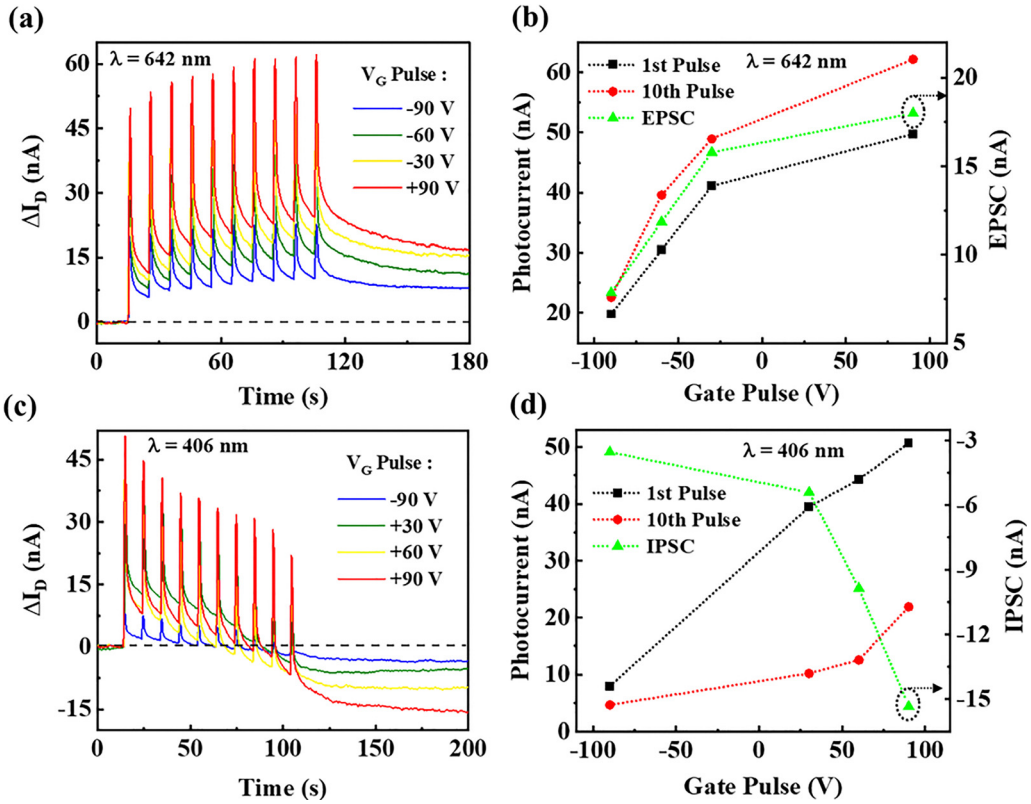

Fig. 3 (a) Gate modulation of synaptic plasticity under 642 nm excitation (pulse duration = 1 s, frequency of 0.1 Hz). (b) Photoresponse measured (under 642 nm) after the 1st and 10th light pulses and EPSC measured after the 10th pulse with respect to gate actuation. (c) Gate modulation of synaptic plasticity under 406 nm excitation. (d) Photoresponse measured (under 406 nm) after the 1st and 10th light pulses and IPSC measured after the 10th pulse with respect to gate actuation.

plays a key role in sustaining the PSC levels over extended periods. This behaviour was confirmed by comparing between the I_D-t measurements (Fig. S7a–c) conducted under 642 nm and 406 nm pulses for $PdSe_2$ and the HS FET. The enhanced photoresponse behaviour (under 642 nm illumination) is further supported by the calculated responsivity (R) and detectivity (D) values of the $PdSe_2$ and the HS FET (Fig. S7a). In particular, the responsivity is measured to be 2.11 A W^{-1} for the HS FET and 0.07 A W^{-1} for the $PdSe_2$ FET. The nearly 30 times increase in responsivity in the HS FET is attributed to the direct bandgap nature of In_2Se_3, which enables superior photon absorption compared to the indirect bandgap of $PdSe_2$.

Detectivity was found to be 0.75×10^{10} Jones for the HS FET and 0.87×10^{8} Jones for the $PdSe_2$ FET, demonstrating that the integration of In_2Se_3 enhances detectivity by nearly two orders of magnitude. It is also important to note that the presented current levels are device specific due to geometry variations of the FET channel area and heterojunction overlap between the In_2Se_3 and the $PdSe_2$ components. All calculated parameters correspond to measurements, that were performed at a drain bias of 100 mV.

Operation mechanism

To understand the bidirectional photoresponse of the device, I_D–V_G measurements were performed under dark and illuminated conditions. As shown in Fig. 4a, the transfer curve consists of a hysteretic loop attributed to both ferroelectric dipole switching and trapping–de-trapping process at the In_2Se_3–$PdSe_2$ interface. Our discussion focuses on the photoresponse at V_G = 0 V as the operational condition relevant for synaptic measurements corresponding to the shaded region in Fig. 4a (magnified in Fig. 4b). The device demonstrates an increase in conductivity under 642 nm light illumination in both sweep directions, indicative of usual positive photoconductive behaviour, in agreement with the observed synaptic response. The magnified view shown in Fig. 4b highlights that the photoresponse following negative poling (forward sweep) is slightly lower than that following positive poling (backward sweep, marked as regions I and II), consistent with the polarization dependent photoresponse results. The PPC effect observed under 642 nm illumination is attributed to both In_2Se_3 and $PdSe_2$, as both materials absorb this wavelength. In particular, photogenerated charges that are absorbed in the In_2Se_3 can transfer to the $PdSe_2$ channel enhancing the overall photoresponse of the device.

The transfer characteristics were also measured under 406 nm light illumination (blue curve in Fig. 4a) to consider the IPSC, where a clear light-induced doping effect is evident, manifested by a leftward shift of the I_D–V_G curve with respect to dark conditions. Such n-type doping effect causes an unusual NPC effect in the $PdSe_2$ channel. Previous studies have reported

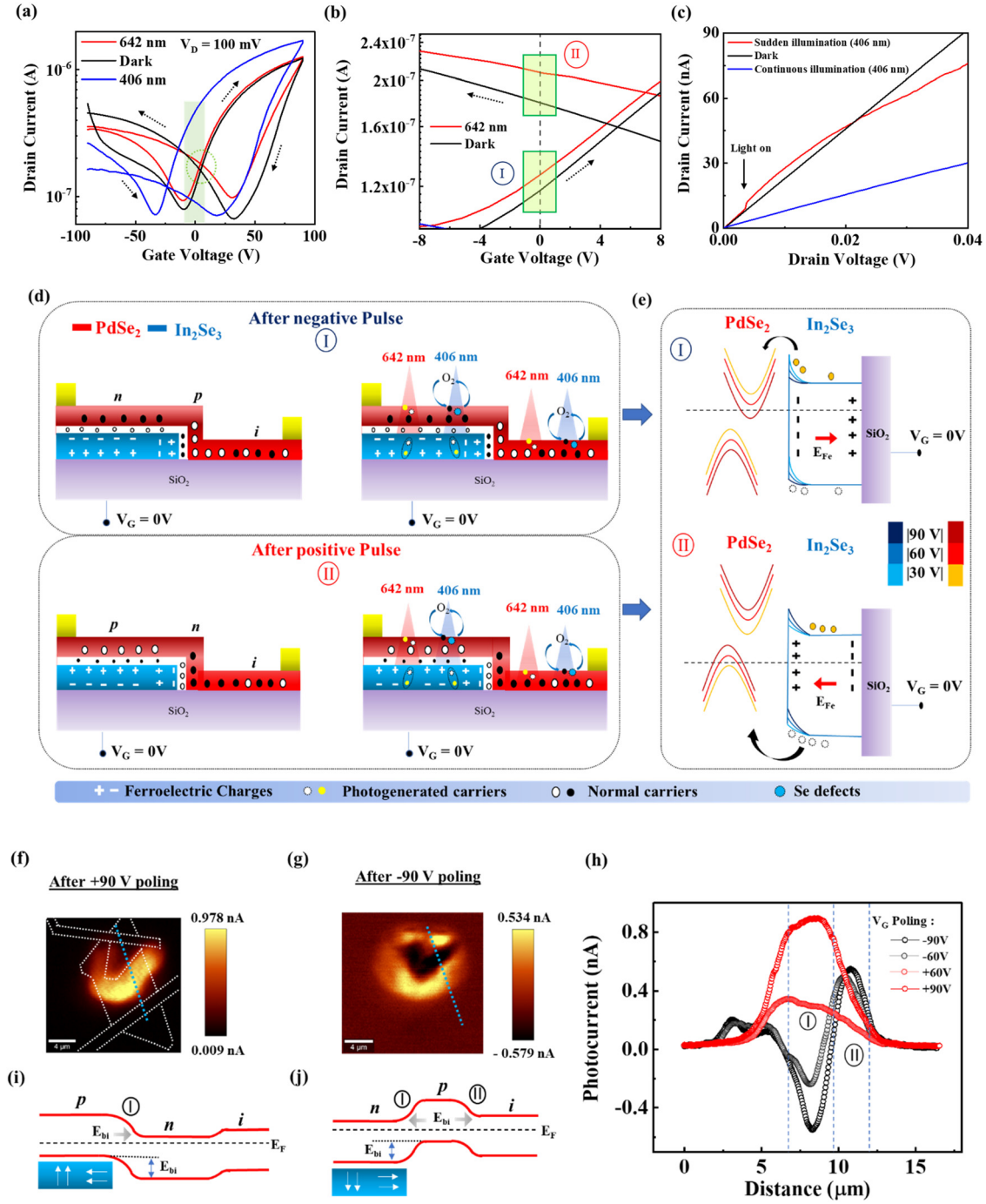

Fig. 4 (a) Transfer characteristic curve under darkness and under light illumination (V_D = 100 mV). (b) Enlarged figure of the circle area in (a). (c) I_D–V_D curve of the device measured under dark, continuous and sudden 406 nm light illumination. Sudden illumination results in instant PPC but a gradual transition to NPC. (d) Schematic representation of the channel conducting state and dipole arrangement following negative (I) and positive (II) gate actuations under dark (left) and light (right) conditions for 642 nm and 406 nm. (e) Energy band diagram of the $PdSe_2$–In_2Se_3 HS interface and charge transfer characteristics of photogenerated carriers following negative (top) and positive (bottom) gate actuations. Solid circles refer to electrons and hollow circles refers to holes. Photocurrent mapping of the device following (f) +90 V gate poling, and (g) −90 V gate poling. (h) Line profiles of the photocurrent along the blue dotted lines in (f) and (g) following ±90 V and ±60 V gate poling. Energy band diagrams of the $PdSe_2$ channel following (i) +90 V gate poling, and (j) −90 V gate poling. Red lines refer to the conduction and valence bands of $PdSe_2$. White arrows in the blue shaded box depict the OOP and IP dipole orientation in In_2Se_3.

that $PdSe_2$ exhibits NPC under shorter visible wavelength illumination by light-induced defect states, resulting in oxygen desorption from its surface.[27,44,54] In particular, 406 nm light illumination causes oxygen adatoms to be ejected from the surface, leaving behind electrons, resulting in an n-type doping effect (Fig. S8). Similarly, high energy photons of short wavelength create

Se vacancy sites, introducing shallow electronic trapping states near the conduction band, resulting in n-type device characteristics.[27,44] Recent experiment and theoretical studies validated the effect of environmental oxygen pressure on this NPC effect in $PdSe_2$ as well as in $PtSe_2$ and $PtTe_2$.[55–57] The degree of doping level with varying light intensity is presented in Fig. S9. I_D–V_D measurements in Fig. 4c further reveal that 406 nm light stimulation induces an instant PPC, mainly attributed to carrier generation in the underlying In_2Se_3. As time progresses, the current decreases below the dark current level, indicating the dominance of the NPC effect from $PdSe_2$. In comparison, a fully symmetric HS device in which $PdSe_2$ is completely supported by In_2Se_3 presents a minor leftward shift in transfer curve under continuous 406 nm light illumination (Fig. S10a), due to the dominant PPC effect by the In_2Se_3. Therefore, by strategically designing a partially covered In_2Se_3 layer by the $PdSe_2$ device, the two opposing photoconductive effects are jointly present, achieving both EPSC and IPSC by optical stimulation.

To interpret the polarization dependent photoresponse and the underlying charge transfer across the In_2Se_3–$PdSe_2$ interface, device configurations for opposite poling conditions under dark and illuminated states are schematically presented in Fig. 4d. Following negative gate poling, the OOP electric dipoles arrange such that they point away from the $PdSe_2$ side, leading to positive holes trapping at the interface between $PdSe_2$ and In_2Se_3 and n-type channel characteristics. Conversely, following positive poling, p-type channel characteristics are introduced. The I_D–V_G curve of the symmetric HS FET similarly confirms that $PdSe_2$, shifts from n-type ambipolarity to p-type ambipolarity following two opposite poling conditions, due to the ferroelectric polarization within the underlying In_2Se_3 (Fig. S10). In addition, in the case of an asymmetric HS FET, the intercoupled IP dipoles form a hole (electron) region in $PdSe_2$ next to the edge of In_2Se_3 following the negative (positive) poling (see the sections below).[39,45,46] Kelvin probe force microscopy (KPFM) was used to determine the relative energy band positions of In_2Se_3 and $PdSe_2$ (Fig. S11). In particular, the Fermi level of In_2Se_3 lies 0.39 eV above Au, while that of $PdSe_2$ is 0.251 eV below In_2Se_3. These relative Fermi level positions in the pristine state are consistent with previous reports based on UPS, KPFM, and theoretical studies.[58–60]

Based on the measured surface potential characteristics of the In_2Se_3–$PdSe_2$ heterojunction, energy band diagrams of the In_2Se_3–$PdSe_2$ interface are depicted in Fig. 4e, where blue and red shaded lines denote the band structure of In_2Se_3 and $PdSe_2$, respectively following different gate-induced ferroelectric polarization. For negative poling, the energy bands of $PdSe_2$ bend downward. As a result, the conduction band of $PdSe_2$ shifts closer to the Fermi level as it forms an n-type channel (as evident by the I_D–V_G profiles of the symmetric HS). Since the work function of $PdSe_2$ is higher than that of In_2Se_3, the energy bands of In_2Se_3 bend upwards, creating a built-in potential at the interface.[59] Under illumination, photogenerated electrons from the In_2Se_3 layer cannot efficiently transfer to the $PdSe_2$ channel due to this potential barrier, resulting in a reduced photoresponse. In contrast, following positive gate poling, the energy bands of $PdSe_2$ bend upward and the valence band becomes close to the Fermi level. Since the FET channel is now formed by holes, photogenerated holes can favourably move across the In_2Se_3–$PdSe_2$ interface leading to a higher photoresponse compared to the negative poling condition.

Depending on the gate poling history, photogenerated charges (e or h), become confined at the interface due to the OOP of In_2Se_3. This attractive field stabilizes the trapped charges for an extended period acting as a virtual gate voltage resulting in a longer PSC in the HS FET. In contrast, in pristine $PdSe_2$ FET, light-induced trapped charges at the $PdSe_2$–SiO_2 interface rapidly decay resulting in the absence of PSC due to the lack of a dipolar field. The role of dipolar field in sustaining the PSC level is further verified by measuring I_D–t in both the symmetric and asymmetric HS FETs (Fig. S7d).

To experimentally validate the above-mentioned device electronic configuration, scanning photocurrent microscopy (SPCM) was performed following different poling conditions (Fig. 4f–h and Fig. S12). During the measurements, the drain bias was kept at 0 V to directly probe the ferroelectrically induced lateral built-in electric fields formed across the $PdSe_2$ channel. A 532 nm laser with an incident power of $\sim$0.3 mW was used to scan the device area. The device geometry is outlined by the white lines in Fig. 4f, and the corresponding optical micrograph and scanned area are presented in Fig. S13a.

Photocurrent maps following +90 V and −90 V poling are shown in Fig. 4f and g, respectively. Fig. 4h shows the corresponding line profiles along the blue dotted path drawn in Fig. 4f and g, where the red and black traces represent positive and negative poling states, respectively. Following positive poling, a positive photocurrent peak is observed next to the In_2Se_3 edge (region I), whereas following negative poling, the photocurrent reverses its direction in region I and an additional positive peak emerges a few microns away from the In_2Se_3 edge (region II). This photocurrent polarity modulation directly stems from the reversal of both IP and OOP ferroelectric dipoles within the underlying In_2Se_3. In particular, under positive poling, OOP dipoles induce a p-type channel within the overlapping HS region, whereas IP dipoles give rise to localized n-type doping in $PdSe_2$ next to the In_2Se_3 edge (region I), forming a p–n junction (Fig. 4i). Given that the native $PdSe_2$ is slightly n-type (Fig. S13b), the influence of IP dipoles can extend further into the $PdSe_2$ channel. Conversely, following negative poling and dipole reversal, an n–p junction is formed and the photocurrent becomes negative (region I in Fig. 4j). Meanwhile, IP dipoles accumulate holes over a limited range, resulting in the formation of a secondary p–i junction at region II, forming a positive photocurrent peak. The observed modulations in the built-in electric fields across the $PdSe_2$ channel confirm the reversal of ferroelectric dipole configuration following alternating gate actuations. Moreover, the evolution of photocurrent amplitude with varying gate-poling voltages (photocurrent maps for $\pm$60 V gate poling conditions are shown in Fig. S13c and d, respectively) is consistent with the device conductive state for different gate voltage sweep ranges, as shown in Fig. S13e and f. Fig. S13b shows negligible hysteresis in the $PdSe_2$ FET, confirming the absence of a non-volatile electrostatic

gating effect at the $PdSe_2/SiO_2$ interface. Moreover, the I_D–t characteristics measured after opposite gate actuations (±90 V) under 642 nm illumination exhibit no significant current variations, indicating that the non-volatile electrostatic gating originates exclusively from the heterostructure region due to dipole switching within the In_2Se_3 (Fig. S14). It is important to note that the electrical measurements of the asymmetric heterostructure were conducted at a low drain voltage (V_D) of 100 mV, where negligible non-linear junction characteristics were observed. However, at higher drain voltages, the device exhibits a mild rectifying behavior due to junctions formation (Fig. S15) indicating that the polarity of the high drain bias (+/−1 V) can affect the overall carrier modulation across the device.[45] Similar electrical and optical characteristics have been observed in other devices (Fig. S16) demonstrating the reproducibility of our results.

Binary logic operation and image recognition

A primary objective of a bidirectional optical synaptic device is to enable SET/RESET operations solely through light stimulation, ensuring a reconfigurable functionality without the reliance on continuous electrical control. Furthermore, integrating Boolean logic operations into such optically controlled synaptic devices would offer significant advantages, particularly for on-chip optical communication and photonic integrated circuits.[20,61] In this section, we demonstrate that the In_2Se_3–$PdSe_2$ synaptic device can be rapidly RESET using high-intensity (>0.17 mW mm^{-2}) 406 nm light, exploiting the NPC effect of $PdSe_2$ at this wavelength, where the ferroelectric nature of In_2Se_3 enables the IPSC to be retained for an extended period of time after light illumination. Hence, a 642 nm light pulse can be employed for optical write operations, while 406 nm light enables the optical erase operation to be performed. Fig. 5a illustrates reconfigurable synaptic operations through optical write and optical erase cycles. Measurements were carried out using a sequence of light pulses from both wavelengths, with no prior application of any poling condition, thereby keeping In_2Se_3 in its natively poled state. It is evident that the transistor "on" state can be effectively switched off within 5 seconds by the application of 406 nm light, demonstrating the optical reset capability of the device. Next, two fundamental logic functions *i.e.*, 'OR' and 'AND' are demonstrated by exploiting the bidirectional photoresponse of this device. Fig. 5b illustrates the experimental concept, where two wavelengths 642 nm and 785 nm, serve as inputs A and B, respectively. Additionally, 406 nm light is employed as a modulatory input to switch the operation from OR to AND. In the input logic scheme, the presence of light is designated as logic "1", whereas the absence of light corresponds to logic "0". For the output logic, a threshold current of 0.55 μA was defined, such that output currents exceeding this threshold are classified as logic "1", while currents below the threshold are classified as logic "0". The output current was measured under a drain bias of 100 mV. As observed in Fig. 5b, when either input A (642 nm) or input B (785 nm) are on (representing 10 or 01 state), the output current exceeds the threshold value, resulting in an output logic of "1". Conversely, when both light inputs are off (00 state), the output current remains below the threshold, yielding an output

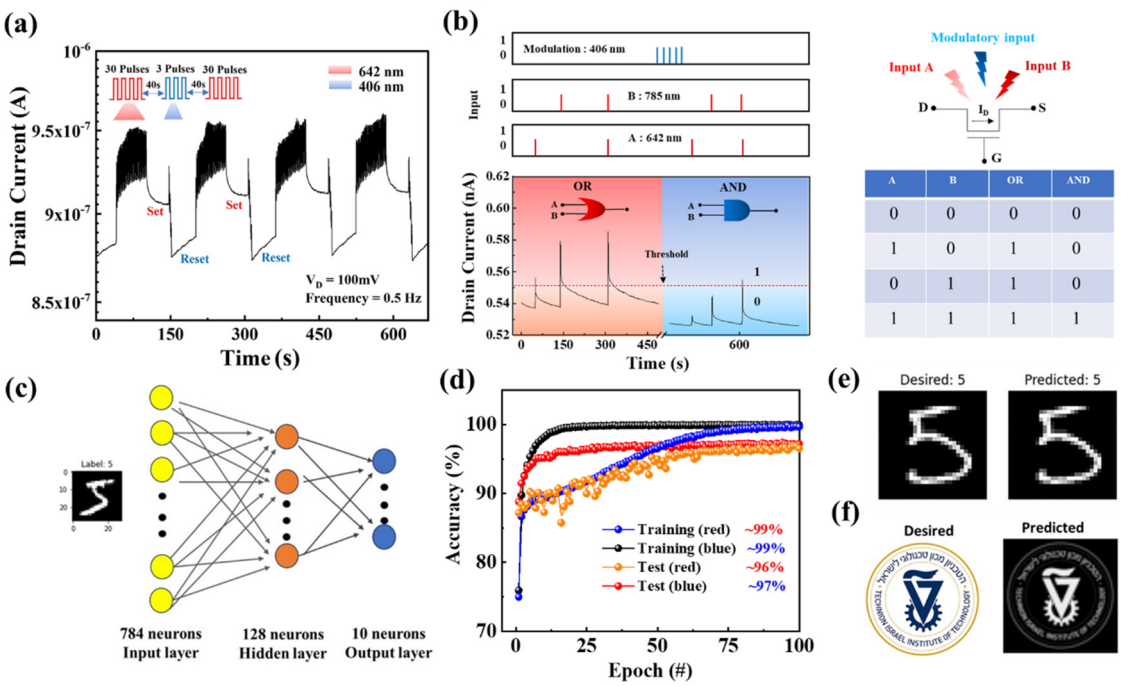

Fig. 5 (a) Optical write & optical erase functionalities with 642 nm and 406 nm light pulses (frequency = 1 Hz) in the unpoled $PdSe_2$–In_2Se_3 HS device. (b) Boolean logic gate operations (OR & AND) with 642 nm and 785 nm as the two input signals and 406 nm as the modulatory input (V_D = 100 mV). (c) Schematic diagram of a three-layer artificial neural network used for simulation of MNIST handwritten digit recognition. (d) The training and test accuracies as a function of the epoch of the 28 × 28 pixel handwritten digit images with red (642 nm) and blue (406 nm) light pulses of 1 Hz frequencies. (e) and (f) The desired and predicted "5' of the MNIST training data set and arbitrary images using a three-layer ANN, respectively.

logic of "0". This behaviour aligns with the truth table of an OR gate. Subsequently, a 406 nm light pulse was applied to reduce the initial current level, enabling the implementation of an AND gate operation. It can be observed that while only one of the inputs, A or B, is active, the output current does not reach the threshold value, whereas when both inputs, A and B, are active (11 state), the threshold is exceeded and thus represents the functionality of an AND gate. Similarly, NOR and NAND gate logic operations can be potentially realized by increasing the initial current level (above 0.55 μA as state '1') using 642 nm laser illumination and then utilizing 406 nm and 520 nm as input A and input B.

Finally, the experimentally observed conductance variations for LTP and LTD (Fig. S17) were directly implemented using a software-based artificial neural network (ANN) to perform neuromorphic simulations. For this purpose, a three-layer ANN was constructed, consisting of an input layer (784 neurons), a hidden layer (128 neurons), and an output layer with 10 neurons representing the class of digits '0'–'9' (Fig. 5c). The hidden layer plays a key role in determining the network performance, as it contains activation functions that process the nonlinear behavior within the ANN. Rectified Linear Units (ReLU) were used as activation functions for the hidden layer, while the 'Adam' optimizer was employed for training the output layer. A 'sparse categorical cross-entropy' loss function was used as the objective function (SI).[62] For neuromorphic simulation, the Modified National Institute of Standards and Technology (MNIST) handwritten digit database was utilized, containing 60 000 grayscale images for training and 10 000 for testing and validation. Fig. 5d presents the training and test accuracies as a function of training epochs. As shown in Fig. 5d and Table S1, the device achieves excellent classification performance for both red (642 nm, 1 Hz) and blue (406 nm, 1 Hz) light-driven device parameters, demonstrating its ability to emulate a bidirectionally optical controlled artificial synaptic system for neuromorphic hardware applications. Interestingly, blue-light-driven recognition achieves its maximum accuracy with fewer epochs than the red-light case (Table S1). This behaviour can be attributed to the experimentally observed conductance response under blue light, which exhibits smaller variations and a more linear modulation behaviour. Finally, the artificial neural network was employed for image recognition, with the desired and predicted images of the digit "5" from the MNIST dataset (Fig. 5e) and for an additional arbitrary image (Fig. 5f), exhibiting near-identical features.

Summary

In summary, we demonstrate a bidirectional optical synapse with ferroelectric assisted tunability based on a vdW HS FET, by partially overlapping $PdSe_2$ on top of ferroelectric In_2Se_3. The device effectively emulates all forms of synaptic plasticity using visible light. Excitatory synaptic behaviour was achieved under illumination at 642 nm, 785 nm, and 980 nm, while inhibitory synaptic behaviour was observed for 520 nm and 406 nm wavelengths. $PdSe_2$ primarily enables an optically induced IPSC to be achieved due to oxygen desorption from its surface under illumination with light at wavelengths of 406 nm and 520 nm. To achieve a balance between PPC and NPC under 406 nm or 520 nm light, a partially overlapping configuration was designed. For both EPSC and IPSC effects, In_2Se_3 plays a crucial role by facilitating photocarrier generation and by controlling interlayer charge separation and channel conductance through dipolar rearrangement. Furthermore, gate induced polarization reversal enables further electrical handle to control the optically induced PSC levels. The precise modulation of synaptic behaviours, achieved through both optical and hybrid optical–electrical inputs, underscores the device suitability for advanced neuromorphic vision systems. This was demonstrated by utilizing the bidirectional photoresponse for a reconfigurable optical-write optical-erase logic platform and image recognition functionality, showcasing its versatility for next-generation neuromorphic hardware systems, on chip optical communication and optoelectronic applications at the nanoscale level.

Experimental section

Sample preparation

In_2Se_3 (HQ Graphene) flakes were directly exfoliated onto a pre-patterned SiO_2 surface using the conventional scotch tape exfoliation method. The first few layers of In_2Se_3 were removed from the bulk crystal to eliminate surface oxide layers and minimize undesirable contamination. Few layers of $PdSe_2$ (HQ Graphene) were exfoliated onto a PDMS stamp, which was mounted onto a glass slide. An optical microscope (Olympus BX53M) equipped with a digital camera (Olympus UC90) was employed to identify suitable flakes. Using a dry transfer technique, selected $PdSe_2$ flakes were precisely aligned and transferred onto the In_2Se_3 surface with the aid of an XYZ micro-manipulator stage attached to the optical microscope.

Device fabrication

A standard electron beam lithography (EBL) technique was employed to define the metal contacts for the drain and source electrodes on the $PdSe_2$ layer using 950 K-poly (methyl methacrylate) (PMMA) resist. After the development of the resist the sample was placed under mild oxygen plasma (Diener PCCE) of 50 W for $\sim$5 seconds to remove unwanted resist residuals. Subsequently, 5 nm Cr and 60 nm Au were deposited onto the sample by electron beam evaporation (Evatec BAK 501A) to serve as electrodes followed by a lift-off process. The deposition rate was set to $\sim$0.5 Å s^{-1} for Cr and to $\sim$1 Å s^{-1} for Au at the base pressure of $\sim 7 \times 10^{-7}$ Torr.

Materials characterization

A standard optical microscope (Olympus BX53M) was used to identify suitable flakes after exfoliation. Morphological study of the device was carried out by Bruker Dimension-Icon Atomic Force Microscopy (AFM) in tapping mode inside a N_2 filled glovebox (H_2O and O_2 content <1 ppm). KPFM was conducted

using frequency modulation (FM KPFM) mode. Pt–Ir-coated n^+-silicon tips (PPP-EFM-50, NANOSENSORS) with 25 nm tip radius were used for surface potential mapping. The electrode on top of the sample was kept grounded during scan *via* a wire bonded PCB board. PFM measurements were conducted under ambient conditions using an Asylum Research/Oxford Instruments MFP-3D Infinity AFM system equipped with a conductive Pt/Ir-coated cantilever (PPP-EFM-50, NANOSENSORS™). In_2Se_3 flakes were mechanically exfoliated onto a conductive substrate comprising 5 nm Cr/50 nm Au deposited on a p^{++} Si/SiO_2 wafer. The tip was operated in contact mode (resonance frequency ~290 kHz) to scan two square regions of different sizes. During scanning, a bias voltage of +6 V and −6 V was applied to the tip while the conductive surface was grounded. The VECTOR PFM mode was used to characterize the OOP ferroelectric domains with a drive amplitude of 3 V and a 1 Hz scan rate. Spectroscopic characterization of the 2D layers and their heterostructure was carried out using a Raman spectrometer (WITec Alpha300R). The measurements were carried out in confocal mode using a 532 nm laser with a 100× objective (NA = 0.9; $\Delta\lambda \approx 360$ nm, 1800 g mm^{-1} grating) lens. The excitation power was typically ~1 mW to avoid any heating and material degradation. SPCM measurements were carried out with same Raman spectrometer setup. The device was scanned with an excitation power of 0.3 mW with a 50× objective (NA = 0.45) lens. An optical chopper (Thorlabs, MC1F10HP) at a frequency of 1500 Hz and a lock in amplifier (Zurich Instruments, MFLI) were used to probe the photocurrent.

Optoelectronic characterization

Electrical and optoelectronic characterization of the fabricated devices were carried out under ambient conditions using a semiconductor parameter analyzer unit (Keysight B1500A) and a probe station (Semishare, SM-4) equipped with an optical microscope. The synaptic measurements were performed using a 4-channel fiber-coupled pulse laser source (model-MCLS1, Thorlabs) focused through a multimode fiber (400 μm core, NA = 0.39, model: M74L, Thorlabs) and a series of adjustable aspheric collimators (models: CFC2-A, CFC2-b and CFC2-C; Thorlabs). Different wavelengths (406 nm, 520 nm, 642 nm, 785 nm, 980 nm) of varying intensities ($P_{d,406\,nm}$: 0.13–0.19 mW mm^{-2}, $P_{d,520\,nm}$: 0.61 mW mm^{-2}, $P_{d,642\,nm}$: 0.04–0.47 mW mm^{-2}, $P_{d,785\,nm}$: 0.35 mW mm^{-2}, $P_{d,980\,nm}$: 0.18 mW mm^{-2}) and pulse width input signals were used for the synaptic measurements. The frequency of laser pulses was modulated with an externally feed-in square waveform generator (Keysight 336000A).

Conflicts of interest

There are no conflicts to declare.

Data availability

The data supporting this article have been included as part of the supplementary information (SI). See DOI: https://doi.org/10.1039/d5mh02349a.

Acknowledgements

E. K. gratefully acknowledges the Israel Department of Energy, the Ministry of Innovation, Science & Technology and the ''Ray and Miriam Klein'' research foundation for financial support.

References

1 G. Migliato Marega, *et al.*, Logic-in-memory based on an atomically thin semiconductor, *Nature*, 2020, **587**, 72–77.
2 S. Mukherjee, D. Dutta, A. Ghosh and E. Koren, Graphene-In2Se3 van der Waals Heterojunction Neuristor for Optical In-Memory Bimodal Operation, *ACS Nano*, 2023, **17**, 22287–22298.
3 T. Zhang, *et al.*, A Reconfigurable All-Optical-Controlled Synaptic Device for Neuromorphic Computing Applications, *ACS Nano*, 2024, **18**, 16236–16247.
4 S. Hadke, M.-A. Kang, V. K. Sangwan and M. C. Hersam, Two-Dimensional Materials for Brain-Inspired Computing Hardware, *Chem. Rev.*, 2025, **125**(2), 835–932.
5 C.-Y. Wang, *et al.*, Gate-tunable van der Waals heterostructure for reconfigurable neural network vision sensor, *Sci. Adv.*, 2020, **6**(26), eaba6173.
6 F. Zhou, *et al.*, Optoelectronic resistive random access memory for neuromorphic vision sensors, *Nat. Nanotechnol.*, 2019, **14**, 776–782.
7 Y.-X. Hou, *et al.*, Large-Scale and Flexible Optical Synapses for Neuromorphic Computing and Integrated Visible Information Sensing Memory Processing, *ACS Nano*, 2021, **15**, 1497–1508.
8 H. Li, *et al.*, Fully photon modulated heterostructure for neuromorphic computing, *Nano Energy*, 2019, **65**, 104000.
9 J. Zeng, *et al.*, Multisensory Ferroelectric Semiconductor Synapse for Neuromorphic Computing, *Adv. Funct. Mater.*, 2024, **34**, 2313010.
10 J. Du, *et al.*, A robust neuromorphic vision sensor with optical control of ferroelectric switching, *Nano Energy*, 2021, **89**, 106439.
11 P. Feng, *et al.*, Self-Powered Optoelectronic Synaptic Devices Based on In2Se3/MoS2 Ferroelectric Heterojunction with Boosted Performance, *Adv. Mater. Technol.*, 2024, **9**, 2301355.
12 X. Li, *et al.*, Multi-Functional Platform for In-Memory Computing And Sensing Based on 2D Ferroelectric Semiconductor α-In2Se3, *Adv. Funct. Mater.*, 2024, **34**, 2306486.
13 L. Hu, *et al.*, Emerging Optoelectronic Devices for Brain-Inspired Computing, *Adv. Electron. Mater.*, 2024, **11**(3), 2400482.
14 J. Sun, *et al.*, Optoelectronic Synapse Based on IGZO-Alkylated Graphene Oxide Hybrid Structure, *Adv. Funct. Mater.*, 2018, **28**, 1804397.
15 Y. Chen, *et al.*, Bidirectional Synaptic Phototransistor Based on Two-Dimensional Ferroelectric Semiconductor for Mixed Color Pattern Recognition, *ACS Nano*, 2023, **17**, 12499–12509.
16 Y. Wang, *et al.*, Negative Photoconductance in van der Waals Heterostructure-Based Floating Gate Phototransistor, *ACS Nano*, 2018, **12**, 9513–9520.
17 S. Seo, *et al.*, Artificial optic-neural synapse for colored and color-mixed pattern recognition, *Nat. Commun.*, 2018, **9**, 5106.

18 R. Yang, *et al.*, All-Optically Controlled Artificial Synapse Based on Full Oxides for Low-Power Visible Neural Network Computing, *Adv. Funct. Mater.*, 2024, **34**, 2312444.
19 X. Zhu and W. D. Lu, Optogenetics-Inspired Tunable Synaptic Functions in Memristors, *ACS Nano*, 2018, **12**, 1242–1249.
20 C. M. Yang, *et al.*, Bidirectional All-Optical Synapses Based on a 2D Bi2O2Se/Graphene Hybrid Structure for Multifunctional Optoelectronics, *Adv. Funct. Mater.*, 2020, **30**, 2001598.
21 L. Wang, *et al.*, Negative Photoconductivity Transistors for Visuomorphic Computing, *Adv. Mater.*, 2024, **36**, 2403538.
22 S. Ge, *et al.*, Bidirectional Photoresponse in Perovskite-ZnO Heterostructure for Fully Optical-Controlled Artificial Synapse, *Adv. Opt. Mater.*, 2022, **10**, 2200409.
23 X. Li, *et al.*, Light-Induced Conductance Potentiation and Depression in an All-Optically Controlled Memristor, *ACS Appl. Mater. Interfaces*, 2024, **16**, 27866–27874.
24 F. Zhou, J. Chen, X. Tao, X. Wang and Y. Chai, 2D Materials Based Optoelectronic Memory: Convergence of Electronic Memory and Optical Sensor, *Research*, 2019, **2019**, DOI: 10.34133/2019/9490413.
25 H. Chen, *et al.*, Logic gates based on neuristors made from two-dimensional materials, *Nat. Electron.*, 2021, **4**, 399–404.
26 T. Ahmed, *et al.*, Fully Light-Controlled Memory and Neuromorphic Computation in Layered Black Phosphorus, *Adv. Mater.*, 2021, **33**, 2004207.
27 J. Jiang, *et al.*, Wavelength-Controlled Photoconductance Polarity Switching via Harnessing Defects in Doped PdSe2 for Artificial Synaptic Features, *Small*, 2024, **20**, 2306068.
28 Y. Lian, *et al.*, Tunable Bi-directional Photoresponse in Hybrid PtSe2− Thin Films Based on Precisely Controllable Selenization Engineering, *Adv. Funct. Mater.*, 2022, **32**, 2205709.
29 S. Katznelson, *et al.*, Bright excitonic multiplexing mediated by dark exciton transition in two-dimensional TMDCs at room temperature, *Mater. Horiz.*, 2022, **9**, 1089–1098.
30 Q. Liang, Z. Chen, Q. Zhang and A. T. S. Wee, Pentagonal 2D Transition Metal Dichalcogenides: PdSe2 and Beyond, *Adv. Funct. Mater.*, 2022, **32**, 2203555.
31 Q. Liang, *et al.*, High-Performance, Room Temperature, Ultra-Broadband Photodetectors Based on Air-Stable PdSe2, *Adv. Mater.*, 2019, **31**, 1807609.
32 Y. Xia, *et al.*, 2D Reconfigurable Memory Device Enabled by Defect Engineering for Multifunctional Neuromorphic Computing, *Adv. Mater.*, 2024, **36**, 2403785.
33 J. Gao, *et al.*, Multifunctional MoTe2 Fe-FET Enabled by Ferroelectric Polarization-Assisted Charge Trapping, *Adv. Funct. Mater.*, 2022, **32**, 2110415.
34 M. H. Pervez, *et al.*, Recent Developments on Novel 2D Materials for Emerging Neuromorphic Computing Devices, *Small Struct.*, 2025, **6**, 2400386.
35 Y. Joo, E. Hwang, H. Hong, S. Cho and H. Yang, Memory and Synaptic Devices Based on Emerging 2D Ferroelectricity, *Adv. Electron. Mater.*, 2023, **9**, 2300211.
36 K. Liu, *et al.*, An optoelectronic synapse based on α-In2Se3 with controllable temporal dynamics for multimode and multiscale reservoir computing, *Nat. Electron.*, 2022, **5**, 761–773.
37 L. Wang, *et al.*, Exploring Ferroelectric Switching in α-In2Se3 for Neuromorphic Computing, *Adv. Funct. Mater.*, 2020, **30**, 2004609.
38 J. Gao, *et al.*, Intrinsic polarization coupling in 2D α-In2Se3 toward artificial synapse with multimode operations, *SmartMat*, 2021, **2**, 88–98.
39 D. Dutta, S. Mukherjee, M. Uzhansky and E. Koren, Cross-field optoelectronic modulation via inter-coupled ferroelectricity in 2D In2Se3, *npj 2D Mater. Appl.*, 2021, **5**, 81.
40 Y. Zhou, *et al.*, Out-of-Plane Piezoelectricity and Ferroelectricity in Layered α-In $_2$ Se $_3$ Nanoflakes, *Nano Lett.*, 2017, **17**, 5508–5513.
41 S. Mukherjee, D. Dutta, M. Uzhansky and E. Koren, Monolithic In2Se3–In2O3 heterojunction for multibit non-volatile memory and logic operations using optoelectronic inputs, *npj 2D Mater. Appl.*, 2022, **6**, 37.
42 S. Mukherjee, *et al.*, Scalable Integration of Coplanar Heterojunction Monolithic Devices on Two-Dimensional In2Se3, *ACS Nano*, 2020, **14**, 17543–17553.
43 S. Mukherjee and E. Koren, Indium Selenide (In2Se3) – An Emerging Van-der-Waals Material for Photodetection and Non-Volatile Memory Applications, *Isr. J. Chem.*, 2022, **62**, e202100112.
44 M. Li, *et al.*, Defect Engineering in Ambipolar Layered Materials for Mode-Regulable Nociceptor, *Adv. Funct. Mater.*, 2021, **31**, 2007587.
45 D. Dutta, *et al.*, Edge-Based Two-Dimensional α-In2Se3–MoS2 Ferroelectric Field Effect Device, *ACS Appl. Mater. Interfaces*, 2023, **15**, 18505–18515.
46 M. Uzhansky, S. Mukherjee, G. Vijayan and E. Koren, Non-Volatile Reconfigurable p–n Junction Utilizing In-Plane Ferroelectricity in 2D WSe2/α-In2Se3 Asymmetric Heterostructures, *Adv. Funct. Mater.*, 2024, **34**, 2306682.
47 M. Uzhansky, A. Rakshit, Y. Kalcheim and E. Koren, Coupled pyroelectric-photovoltaic effect in 2D ferroelectric α-In2Se3, *npj 2D Mater. Appl.*, 2025, **9**, 6.
48 F. Guo, *et al.*, Achieving reinforcement learning in a three-active-terminal neuromorphic device based on a 2D vdW ferroelectric material, *Mater. Horiz.*, 2023, **10**, 3719–3728.
49 S. Wan, *et al.*, Room-temperature ferroelectricity and a switchable diode effect in two-dimensional α-In2Se3 thin layers, *Nanoscale*, 2018, **10**, 14885–14892.
50 Y. Zhou, *et al.*, Out-of-Plane Piezoelectricity and Ferroelectricity in Layered α-In2Se3 Nanoflakes, *Nano Lett.*, 2017, **17**, 5508–5513.
51 C. Zheng, *et al.*, Room temperature in-plane ferroelectricity in van der Waals In_2Se_3, *Sci. Adv.*, 2018, **4**, eaar7720.
52 F. Xue, *et al.*, Room-Temperature Ferroelectricity in Hexagonally Layered α-In2Se3 Nanoflakes down to the Monolayer Limit, *Adv. Funct. Mater.*, 2018, **28**, 1803738.
53 W. F. Io, *et al.*, Temperature- and thickness-dependence of robust out-of-plane ferroelectricity in CVD grown ultrathin van der Waals α-In2Se3 layers, *Nano Res.*, 2020, **13**, 1897–1902.
54 A. N. Hoffman, *et al.*, Exploring the air stability of PdSe2 via electrical transport measurements and defect calculations, *npj 2D Mater. Appl.*, 2019, **3**, 50.

55 A. Grillo, *et al.*, Coexistence of Negative and Positive Photoconductivity in Few-Layer PtSe2 Field-Effect Transistors, *Adv. Funct. Mater.*, 2021, **31**, 2105722.
56 S. S. Han, *et al.*, Wafer-Scale Anion Exchange Conversion of Nonlayered PtS Films to van der Waals Two-Dimensional PtTe2 Layers with Negative Photoresponsiveness, *Chem. Mater.*, 2022, **34**, 6996–7005.
57 S. S. Han, *et al.*, Wafer-scale flexible 2D PtSe2 layers with bi-directional wavelength tunability for fully optical synaptic operations, *Nano Energy*, 2025, **139**, 110943.
58 S. M. Poh, *et al.*, Molecular-Beam Epitaxy of Two-Dimensional In2Se3 and Its Giant Electroresistance Switching in Ferroresistive Memory Junction, *Nano Lett.*, 2018, **18**, 6340–6346.
59 Y. Mu, *et al.*, Homo-type α-In2Se3/PdSe2 Ferroelectric van der Waals Heterojunction Photodetectors with High-performance and Broadband, *Adv. Funct. Mater.*, 2024, **34**, 2315543.
60 H. Kim and H. J. Choi, Quasiparticle band structures of bulk and few-layer \mathrmPdSe_2 from first-principles GW calculations, *Phys. Rev. B*, 2021, **103**, 165419.
61 M. A. Zidan, J. P. Strachan and W. D. Lu, The future of electronics based on memristive systems, *Nat. Electron.*, 2018, **1**, 22–29.
62 J. J. Ryu, *et al.*, Highly Linear and Symmetric Weight Modification in HfO2-Based Memristive Devices for High-Precision Weight Entries, *Adv. Electron. Mater.*, 2020, **6**, 2000434.